Transition between quasi-two-dimensional and three-dimensional Rayleigh-Bénard convection in a horizontal magnetic field

Tobias Vogt,[1] Wataru Ishimi,[2] Takatoshi Yanagisawa,[3] Yuji Tasaka,[2] Ataru Sakuraba,[4] and Sven Eckert[1]

[1]*Helmholtz Zentrum Dresden-Rossendorf (HZDR), Dresden, Germany*
[2]*Laboratory for Flow Control, Hokkaido University, Sapporo, Japan*
[3]*Japan Agency for Marine-Earth Science and Technology (JAMSTEC), Yokosuka, Japan*
[4]*Department of Earth and Planetary Science, University of Tokyo, Tokyo, Japan*

Magnetohydrodynamic Rayleigh-Bénard convection was studied experimentally and numerically using a liquid metal inside a box with a square horizontal cross section and an aspect ratio of 5. Applying a sufficiently strong horizontal magnetic field converts the convective motion into a flow pattern of quasi-two-dimensional (quasi-2D) rolls arranged parallel to the magnetic field. The aim of this paper is to provide a detailed description of the flow field, which is often considered as quasi-2D. In this paper, we focus on the transition from a quasi-two-dimensional state toward a three-dimensional flow occurring with decreasing magnetic-field strength. We present systematic flow measurements that were performed by means of ultrasound Doppler velocimetry. The measured data provide insight into the dynamics of the primary convection rolls, the secondary flow induced by Ekman pumping, and they reveal the existence of small vortices that develop around the convection rolls. New flow regimes have been identified by the velocity measurements, which show a pronounced manifestation of three-dimensional flow structures as the ratio Ra/Q increases. The interaction between the primary swirling motion of the convection rolls and the secondary flow becomes increasingly strong. Significant bulging of the convection rolls causes a breakdown of the original recirculation loop driven by Ekman pumping into several smaller cells. The flow measurements are completed by direct numerical simulations. The numerical simulations have proven to be able to qualitatively reproduce the newly discovered flow regimes in the experiment.

I. INTRODUCTION

One of the classical problems in fluid dynamics is Rayleigh-Bénard convection (RBC), where a fluid layer is exposed to a temperature difference ΔT between a colder lid and a warmer bottom. Various RBC regimes are defined by the Rayleigh number, Ra $= \alpha g \Delta T H^3 / \kappa \nu$, the Prandtl number, Pr $= \nu / \kappa$, and the geometry of the fluid vessel. In these formulae, α, κ, and ν are the volumetric coefficient of thermal expansion, thermal diffusivity, and kinematic viscosity of the fluid, respectively, and g and H represent the gravity acceleration and height of the fluid layer, respectively. Numerous studies about RBC have been published, and an introduction and overview can be found in [1,2]. Effects arising from external forces such as magnetic fields [3,4] or vessel rotation [5,6] have attracted a growing interest among the scientific community. For instance, an extension of the Lohse-Grossmann theory to the magnetohydrodynamic (MHD) case has been suggested recently [7]. The present experimental and numerical study considers the specific case of liquid-metal convection exposed to a dc magnetic field [8]. RBC under the influence of a steady magnetic field is of particular interest in geo- and astrophysics [9], but it also has some relevance for technical applications such as the use of liquid metals for heat removal in fusion blankets [10]. The effect of the magnetic field

is quantified by the dimensionless Chandrasekhar number $Q = B^2 H^2 \sigma / \rho \nu$, which is the Hartmann number Ha squared. It represents the ratio of the electromagnetic force to the viscous force, where σ and ρ are the electric conductivity and the density of the fluid, respectively, and B is the strength of the applied magnetic field. The magnetic field in our experiments is applied in a horizontal direction perpendicular to the temperature gradient. A sufficiently strong magnetic field causes a two-dimensional convection pattern such that the convection rolls are oriented along the magnetic-field lines. The corresponding flow regime diagram of the convection patterns was reported in a recent paper [11]. This regime diagram reveals a multitude of flow structures governed by the balance between the Lorentz force and the buoyancy, and it illustrates the selection criterion for the roll number depending on Ra and Q. Further previous studies presented essential features of various regimes and regime transitions, including the characteristic phenomena of "flow reversals" emerging at specific selections of Ra and Q [12–14]. These flow reversals are distinguished by spontaneous changes of the rotational direction of the convection rolls, and they might be caused by the oscillatory instability and the skewed-varicose instability, both of which affect the quasi-two-dimensional rolls. In continuation of this previous work, we focus in this paper on the identification and qualitative description of specific flow structures occurring during the transition from a steady quasi-two-dimensional roll pattern to transient three-dimensional regimes by lowering the magnetic field or increasing the Ra number.

In general, the application of the dc magnetic field generates a Lorentz force that strongly attenuates angular momentum perpendicular to the field lines by Joule dissipation [15]. The Joule dissipation would become noneffective for a perfectly two-dimensional (2D) configuration of an infinite roll length, where the electrical potential cannot drive current loops. Due to this mechanism, the flow field tends to become uniform along the magnetic-field direction. However, the anisotropy of the flow field does not necessarily mean that the velocity component parallel to the field vanishes. Since we consider the convection in a box with a square cross section, the convection rolls are confined by no slip boundaries. The differential rotation of the fluid particles at those solid walls at the end of the convection rolls produces a converging flow in the boundary layer, called Ekman pumping [16]. The interaction of a vortex flow with a plane surface is called the Bödewadt problem [17]. The thickness of the related Bödewadt layer follows from the relation $\delta_B \sim (\nu/\Omega)^{1/2}$, where Ω stands for the rotation rate of the convection rolls. Due to continuity, the Ekman pumping is responsible for driving a secondary loop inside the fluid vessel. In the flow configuration considered here, the Ekman pumping happens at the sidewalls perpendicular to the magnetic-field lines. Hence, the near-sidewall region is also covered by the Hartmann layers where the electromagnetic force and viscous friction balance each other out. Because the side walls perpendicular to the magnetic field are electrically nonconducting in our experiment, the induced electric currents close exclusively within the Hartmann layers [3]. These Hartmann layers are in the order of $O(Ha^{-1})$ [18] and become quite thin for high Hartmann numbers. Their influence on the flow has to be considered in relation to the boundary layers created by Ekman pumping. A detailed theoretical analysis of Ekman pumping in these Bödewadt-Hartmann layers was performed in [19]. Furthermore, a recent study considered the role of Ekman pumping in the context of the dimensionality of a single electrically driven vortex bounded by two horizontal walls [20].

For decreasing intensity of the magnetic field at a given Ra number, an initially stable quasi-2D structure of convection rolls arranged parallel to the magnetic field will become unstable and tend to develop 3D perturbations. The secondary flow generated by Ekman pumping is supposed to play an essential role during the transition from a quasi-two-dimensional toward a three-dimensional flow field.

There is still rather limited knowledge concerning the development of 3D flow structures in RBC under the impact of a horizontal dc magnetic field. In this paper, we provide a detailed representation of 3D flow structures by measuring the spatiotemporal flow velocity maps parallel and perpendicular to the magnetic-field lines. The flow velocities are acquired by means of ultrasound-Doppler-velocimetry (UDV), which is an attractive tool for visualizing flow patterns in opaque fluids such as liquid metals. The experimental work is complemented by direct-numerical simulations, which enable a more intuitive understanding of the complex flow structures.
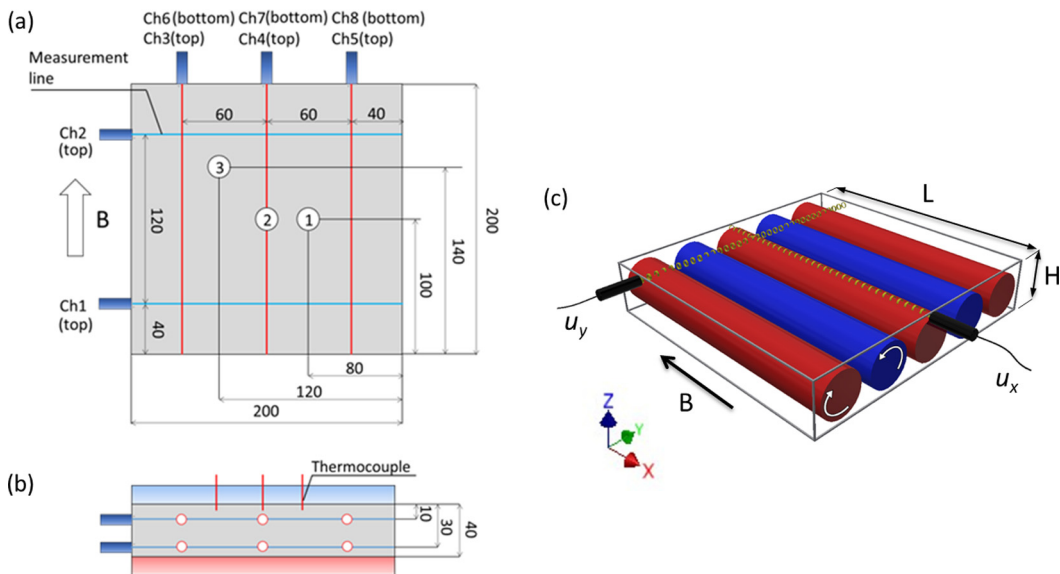
FIG. 1. Experimental setup: top view (a) and side view (b). The dimensions are in mm. Schematic drawing of the counter-rotating convection rolls and UDV measuring lines (c).

II. EXPERIMENTAL SETUP AND NUMERICAL SIMULATION

A. Experimental setup and procedure

The temperature and flow measurements reported within this paper were conducted by means of the same experimental setup as was used in a previous work [14]. The eutectic alloy GaInSn, which has a melting temperature of $T_0 = 10.5\,°C$, is filled in a rectangular vessel with an inner cross section of 200 mm × 200 mm and a height of 40 mm, giving an aspect ratio of 5 (see Fig. 1). At room temperature, the metal alloy has approximately one-third the viscosity of water ($\nu = 3.4 \times 10^{-7}\,m^2/s$), a density of $\rho = 6360\,kg/m^3$, and an electrical conductivity of $\sigma = 3.2 \times 10^6\,S/m$. The thermal diffusivity is $\kappa = 1.05 \times 10^{-5}\,m^2/s$ and the thermal expansion coefficient is $\alpha = 1.24 \times 10^{-4}\,1/K$ [21]. Accordingly, the Pr number is about 0.03. The sidewalls of the insulating vessel are made of polyvinyl chloride (PVC), whereas the top and bottom plate are made of copper. The temperature of both copper plates can be controlled by water that is pumped through channels inside the plates. The copper plates have about 20 times the thermal conductivity of GaInSn. The filled vessel is located inside a dc inductor that creates a horizontal magnetic field up to 350 mT. Measurements of the field strength showed nonuniformities less than 5% throughout the measuring volume.

Two of the vessel sidewalls are equipped with ultrasound transducers (Ch1–Ch8, see Fig. 1) in order to measure both components of the fluid velocity parallel and perpendicular to the magnetic-field lines. The transducers are connected to a DOP 2000 velocimeter (model 2125, Signal Processing SA, Lausanne). The spatial resolution of the velocity measurements is about 1 mm in the axial direction and 5 mm in the lateral direction, whereas a temporal resolution of about 1 Hz has been realized. The transducers are in direct contact with the fluid in order to ensure a good acoustic transmission for enabling the acquisition of velocity data with satisfying quality even at low liquid velocities of about 0.5 mm/s. The applied sensor positions are shown in Figs. 1(a) and 1(b). We used custom-built transducers (Fa. Richter STT) made without any ferromagnetic parts in order to avoid any interference of the measuring signal by the strong magnetic field.

The temperatures of the bottom and top plates were measured with one thermocouple each embedded in the copper plates. The temperatures inside the fluid were measured at three different

positions (see Fig. 1) at a 3-mm distance from the upper boundary by means of thermocouples as well. The temporal resolution of the temperature measurements is about 10 Hz.

B. Method of numerical simulation

We performed direct numerical simulations for the same geometry as in the laboratory experiment, considering a horizontal magnetic field imposed on the rectangular vessel of no-slip velocity boundaries. The main motivation for the numerical simulation was to improve the understanding of the complex 3D effects, especially by revealing the complete flow structure in the entire vessel. The numerical code used here is identical to that in [13], and it reproduced successfully the diverse convection regimes observed experimentally for variations of Ra and Q. In the code, a set of governing equations for magnetohydrodynamic flows is solved for a Boussinesq fluid. The second-order accurate staggered-grid finite-difference method is applied using a uniform grid interval. The time integration was performed explicitly by means of the third-order Runge-Kutta method. The selected number of vertical grid points is 48, 64, and 120, depending on the value of Ra and Q. As the aspect ratio of the vessel is 5, this gives 240, 320, and 600 horizontal grid points for an equidistant mesh. The choice of the grid resolution is a compromise between a sufficient number of grid points in the Hartmann layer and a reasonable computation time. In this study, the calculations for the highest Chandrasekhar number of $Q = 5.7 \times 10^3$ were conducted on a mesh of $600 \times 600 \times 120$ grid points. To check the reliability of the results, additional calculations were performed for the same Q at a finer mesh doubling the grid points in all three directions to $1200 \times 1200 \times 240$. The comparison of the results shows a better resolution of finer flow structures by the denser mesh, but it does not reveal significant discrepancies with respect to the main flow structure. Between these two cases, the relative difference in the time-averaged value of the Nusselt number is in the order of 10^{-4}, and that of the oscillation period is ~ 0.01. The value of the Pr number for the simulations was set to 0.025. In these simulations, the length and time are nondimensionalized by the layer thickness H and the thermal diffusion time $\tau_\kappa = H^2/\kappa$, respectively. The time unit corresponds to $\tau_\kappa = 152\,\mathrm{s}$ and the velocity unit to $U = H/\tau_\kappa = 0.26\,\mathrm{mm/s}$. For more details and information with respect to a verification of the code, the reader is referred to [13].

III. RESULTS

Figure 2(a) shows the regime diagram replotted from [14]. In contrast with that previous paper, here we use material property data for GaInSn taken from a more recent publication [21]. Depending on the choice of Ra and Q, diverse flow regimes can be observed ranging from an isotropic pattern without a preferred orientation of the convection rolls through six-roll structures strictly aligned parallel to the magnetic field. Previous studies indicate that the transitions between the main regimes obviously occur along lines of Ra/Q = const [11,13,14]. Above Ra/Q = 100, the magnetic field appears to be too weak to provoke any significant changes of the isotropic flow pattern. Here, the convection rolls do not show a preferred orientation. Below Ra/Q = 100, the convection rolls become aligned parallel to the magnetic-field lines. The first stable flow configuration that can be observed in our system at Ra/Q < 100 is a four-roll configuration. If the magnetic field is further increased (Ra/Q < 10), the most stable flow configuration is found at five rolls. As soon as the magnetic field aligns the convection rolls with the magnetic-field lines, the flow components perpendicular to the magnetic field become dominant, whereas the flow parallel to B is significantly weaker. The latter, however, is not negligible. To reconstruct a complete figure of the considered flow, both velocity components parallel and perpendicular to the magnetic field have been measured. Prominent features of the flow structure will be discussed below.

Figure 2(b) contains a section of the regime diagram showing the parameter range covered by this study. In this paper, we selected exemplary cases for studying the gradual loss of stability of the quasi-2D roll pattern with decreasing impact of the magnetic field. For that purpose, we increased stepwise the ratio Ra/Q and focused especially on measurements of the axial velocity u_x parallel to
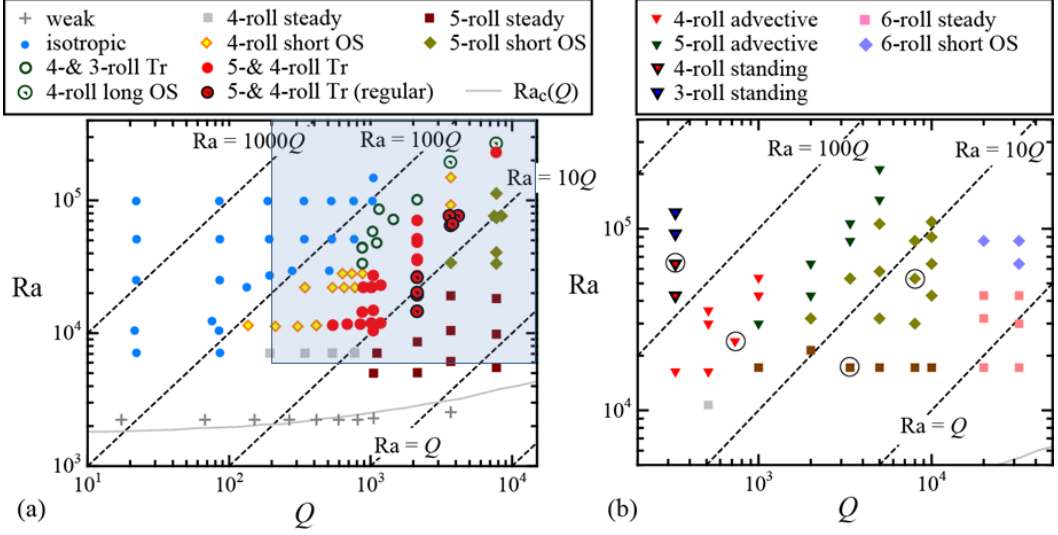
FIG. 2. (a) Regime diagram of the liquid-metal RBC exposed to a horizontal magnetic field replotted from [14], where the gray line represents the expected neutral stability curve for the vessel with an aspect ratio of 5 based on the result in [3]; abbreviations: OS, oscillation; Tr, transition (transition means here the switching between different roll number states). (b) Parameter points of flow measurements carried out within this study, whereas the circled symbols mark the measurements to be presented in the next paragraph. The overlap between both diagrams is marked by the gray rectangle in (a).

convection rolls. These measurements allow for the detection of early deviations from the 2D state since any velocity gradient emerging along the magnetic field becomes immediately visible and is not overlaid by the mean flow. The particular measurements to be presented in the next section are highlighted by encircled symbols. On the route from quasi-2D structures to 3D ones, we identified four different regimes on the basis of flow measurements along the direction of the magnetic field. Referring to data obtained by the measurements perpendicular to the field, the flow structure can be classified being a four-roll short oscillation (OS) regime according to Fig. 2(a) and already known from former studies. The analysis of the axial flow component discloses that this regime can be subdivided into two additional regimes. While the oscillations of the primary flow structure remain two-dimensional for $Ra/Q < 10$, two new regimes have been identified for $Ra/Q \geqslant 30$, called the four-roll advective regime and the four-roll standing-wave regime, respectively. Here, the flow measurements demonstrate clear deviations from two-dimensionality. Although not shown as flow measurement in this paper, a three-roll standing-wave regime is also newly observed for $Ra/Q > 300$.

A. Velocity measurements

Figure 3(a) shows a measurement of the u_y component (perpendicular to B) of a stable five-roll configuration, which is an example of the "five-roll steady" regime. This dataset was recorded along the measuring line of Ch2 [see Fig. 1(a)] at $Ra = 1.7 \times 10^4$ and $Q = 3.4 \times 10^3$, which corresponds to $Ra/Q = 5.1$. A negative velocity (blue) indicates a flow toward the sensor, while positive velocities (red) stand for movements away from the sensor. The maximal velocity in Fig. 3(a) is about $\pm 4.7\,\text{mm/s}$, whereby the measuring line is 10 mm above the roll center. Thus, the angular speed of the roll can be estimated to be $\omega \approx 4.7\,\text{mm/s} \times (2\pi \times 10\,\text{mm})^{-1} = 0.075\,\text{Hz}$, leading to a circulation period of about 13 s for one rotation.

Figure 3(b) shows the velocity components parallel to the magnetic-field lines (u_x) measured by Ch7 [see Fig. 1(a)]. It reveals a two-cell structure being symmetric with respect to the middle of the fluid vessel. The velocities parallel to B reach values around 1/6th of the velocities perpendicular
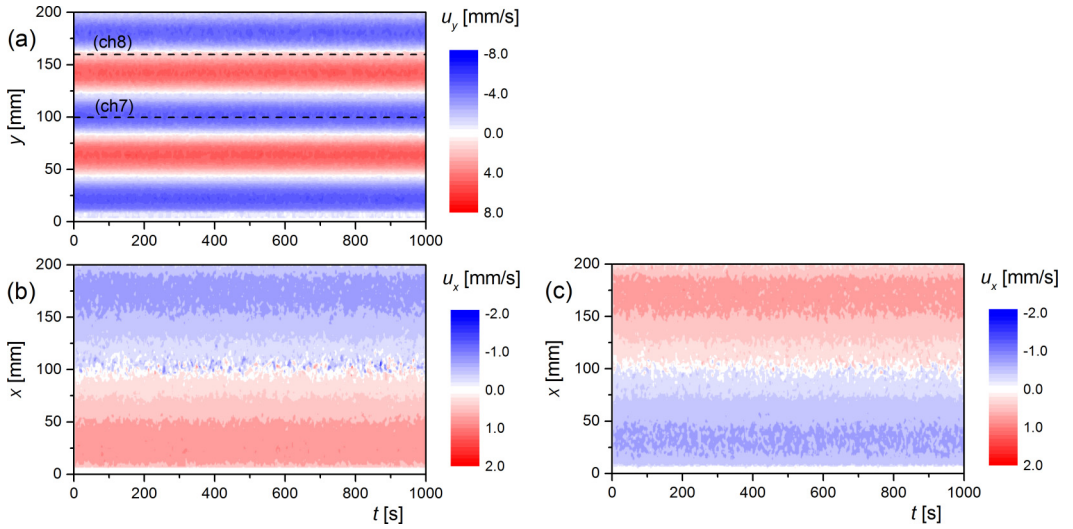
FIG. 3. Flow measurement of a five-roll steady regime at Ra/Q = 5.1 ($Q = 3.4 \times 10^3$, Ra = 1.7×10^4). (a) (Ch2): Fluid velocity perpendicular to the magnetic field, (b) (Ch7), and (c) (Ch8): fluid velocity measured along the magnetic-field lines.

to B. A similar symmetric distribution of the velocity components parallel to the magnetic-field lines is obtained at the other UDV channel, Ch8, as shown in Fig. 3(c). The magnitude of the velocity is almost the same as for Ch7, but the flow direction is completely the opposite. The transducer positions Ch7 and Ch8 are marked in Fig. 3(a) by dashed lines. In a five-roll arrangement, the position of transducer Ch7 coincides with the middle of the third convection roll, whereas the measuring line for Ch8 proceeds almost exactly between two neighbouring convection rolls. Figures 3(b) and 3(c) demonstrate that inside the convection rolls, the secondary flow parallel to the magnetic field is directed from the Bödewadt layers toward the center of the fluid vessel, and it comes back to the wall along the rim of rolls.

Figure 4 shows a measurement obtained at a slightly higher Ra/Q ratio, at Rayleigh number Ra = 5.5×10^4 and Chandrasekhar number $Q = 8.0 \times 10^3$. The higher-temperature difference imposed here results in higher fluid velocities compared to the experiment presented in Fig. 3. On the other hand, the increased magnetic-field strength stabilizes the convection rolls. A detailed consideration of Fig. 4(a) reveals a slight but regular oscillation that appears in both flow directions (u_y and u_x). This case belongs to the "five-roll short OS" regime. This oscillation can be associated with a deformation of the rolls from a circular toward an elliptical cross section [14].
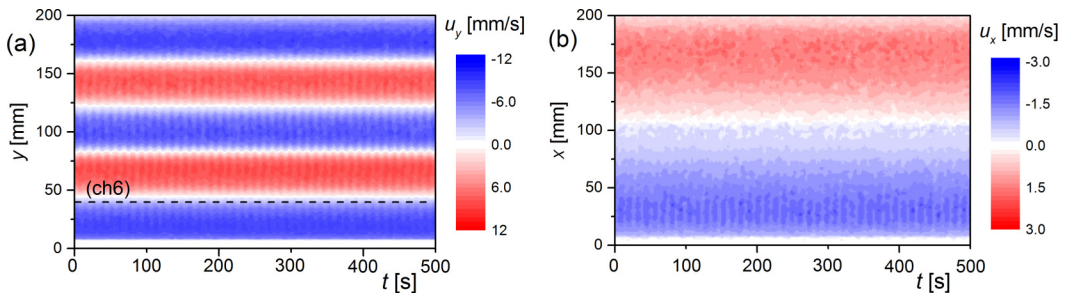

FIG. 4. Flow measurement of a five-roll regime showing short-period oscillations at Ra/Q = 6.9 ($Q = 8.0 \times 10^3$ and Ra = 5.5×10^4). (a) (Ch2) Fluid velocity perpendicular to the magnetic field, (b) (Ch6) fluid velocity measured along the magnetic-field lines.
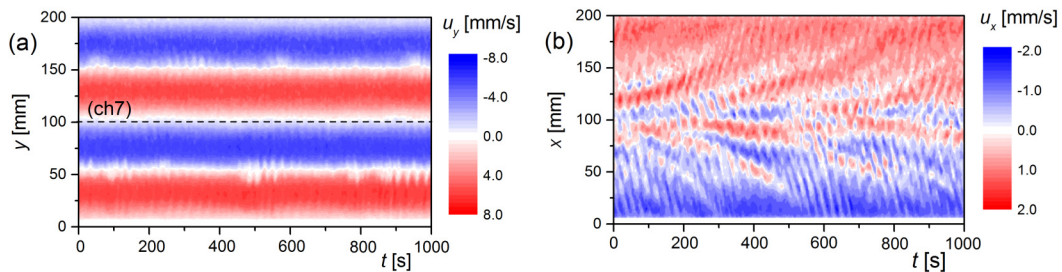
FIG. 5. Flow measurement of a four-roll regime showing advective transport of flow structures along the magnetic-field direction at Ra$/Q = 33$ ($Q = 7.3 \times 10^2$ and Ra $= 2.4 \times 10^4$). (a) (Ch2) Fluid velocity perpendicular to the magnetic field, (b) (Ch7) fluid velocity measured along the magnetic-field lines.

Figure 4(b) shows the flow field parallel to the magnetic field measured by transducer Ch6. The ratio of the velocities u_x/u_y is about 1/5 and the appearance of short-period oscillation can also be seen here. The basic structure of the flow field in the direction of B remains the same, as shown in Figs. 3(b) and 3(c).

The measurement shown in Fig. 5 was recorded at a distinctly higher Ra$/Q$ ratio of 33 ($Q = 7.3 \times 10^2$ and Ra $= 2.4 \times 10^4$). Hence, the stabilizing effect of the magnetic field becomes weaker. The increase of Ra$/Q$ is associated with a change of the convection pattern to a four-roll configuration. The most significant change, however, can be detected in the u_x velocity field [see Fig. 5(b)]. The flow field in the direction of B is now superimposed by some vortex substructures that emerge in the center of the cell. After their formation, the vortices are captured by the diverging axial flow and are transported toward either of the sidewalls of the cell. This is a significant feature of the newly identified "four-roll advective" regime. Obviously, the sideward movement of the emerging vortices occurs in alternating directions, and the advection speed of the vortices increases the closer they come to the sidewalls, as indicated by the curved path of the vortices. The visual manifestation of the vortices in this spatiotemporal velocity plot and their behavior in the axial recirculation shows distinct similarities to Taylor-Görtler vortices in a transitional rotating liquid-metal flow that was driven by a rotating magnetic field [22].

In contrast to the u_x velocity field, the vortices are not visible in the u_y velocity field [see Fig. 5(a)]. The configuration of the four convection rolls looks rather stable. Only some weak disturbances appear between neighboring rolls. Short-term oscillations of the flow become visible just as in the case of the five-roll regime at lower Ra$/Q$ in Fig. 4. These oscillations appear to be much more pronounced in the axial flow shown in Fig. 5(b). The ratio of the velocities u_x/u_y is also about 1/5, as in Fig. 4.

A further increase of Ra$/Q$ to a value of 203 leads to the flow pattern displayed in Fig. 6 ($Q = 3.3 \times 10^2$ and Ra $= 6.7 \times 10^4$). In the regime diagram shown in Fig. 2(a), this Ra$/Q$ ratio is associated
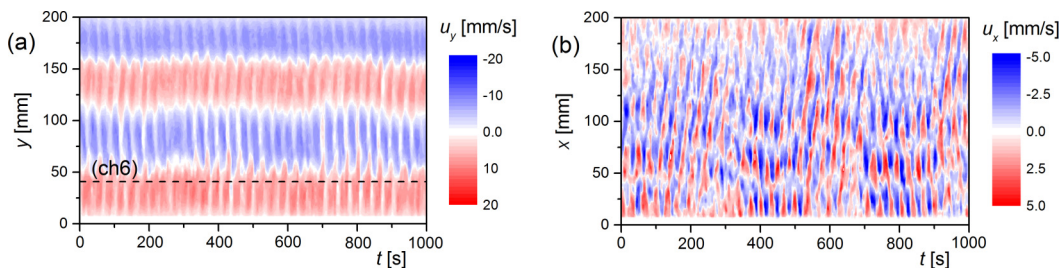

FIG. 6. Flow measurement of a four-roll regime showing the occurrence of standing waves in both velocity components at Ra$/Q = 203$ ($Q = 3.3 \times 10^2$ and Ra $= 6.7 \times 10^4$). (a) (Ch2) Fluid velocity perpendicular to the magnetic field, (b) (Ch6) fluid velocity measured along the magnetic-field lines.

with the "isotropic" domain of thermal turbulence where the flow is expected to lose its orientation with respect to the direction of B. However, the flow in Fig. 6 cannot be classified as fully isotropic since the roll structure still exists in this state [see Fig. 6(a)]. It was observed that the four-roll structure is kept for this region. Strong oscillations of the roll intensity become apparent showing significantly larger periods than the oscillating pattern in Fig. 4. In addition to these almost regular fluctuations, a long-period modulation with respect to the roll size and position can be noticed. Looking at Fig. 6(b) makes it clear that the structure of the axial flow component is dominated by the same type of oscillations. We suggest ascribing these flow features to the occurrence of standing waves in this parameter region. We classified this case as a "four-roll standing-wave" regime. The ratio of $u_x/u_y = 1/2$ in Fig. 6 is considerably higher, as in the examples shown before. The spatiotemporal structure of the axial flow parallel to the magnetic field can be divided into four or five subdomains where the flow direction changes periodically. Apparently, this behavior is synchronized with slight modulations in the main roll structure. We observed similar standing waves accompanied by the three-roll structure at higher Ra/Q, as indicated in Fig. 2(b). All in all, these observations provide strong indications of a flow transition from a quasi-two-dimensional to a three-dimensional state.

B. Temperature measurements

In the previous section, four different flow regimes were identified by the velocity measurements in Figs. 3–6. Figures 7(a)–7(d) show a set of temperature measurements conducted simultaneously to these four flow measurements. From the time series of the temperature recorded at the sensor position 2, one can distinguish four different temperature regimes as well [Figs. 7(a)–7(d)]. For the lowest value of Ra/$Q = 5.1$, the temperature in the fluid is almost constant, and the fluctuations in the signal are apparently caused by noise [Fig. 7(a); five-roll steady]. This regime, which has been associated with the existence of stationary rolls, does not exhibit clear peaks in the fast Fourier transform (FFT) analysis as shown in Fig. 7(e). Distinct oscillations can be observed for Ra/$Q = 6.9$ [Fig. 7(b); five-roll short OS]. The frequency peak $f_{OS} = 0.084$ Hz and its harmonics, e.g., $2f_{OS}$, in Fig. 7(f) correspond very well to the oscillation frequency of the convection rolls detected by the velocity measurements in Fig. 4.

These so-called short-period oscillations become more irregular and are superimposed by some long-period fluctuations if the ratio Ra/Q is further increased [Fig. 7(c); four-roll advective]. This results in a widening of the peak $f_{OS} = 0.03$ Hz and its harmonics. Additionally, the low-frequency modulation of the temperature signal appears in the form of a higher amplitude at the low-frequency range $f \approx 2 \times 10^{-3}$ Hz illustrated by the temperature spectrum in Fig. 7(g). This fact could be explained by the slow propagation of structures along the convection rolls [see Fig. 5(b)].

The amplitude of the temperature fluctuations becomes larger and their shape looks quite irregular at the highest value of Ra/Q considered here [Fig. 7(d); four-roll standing]. Both frequencies f_{OS} and $2 \times f_{OS}$ can still be identified as singular peaks by the FFT, whereas their width increases further [Fig. 7(h)].

The development of temperature fluctuations observed within this study is rather similar to corresponding results reported in [3] for a wider container.

IV. DEVELOPMENT OF THE FLOW STRUCTURE DURING THE TRANSITION FROM A QUASI-TWO-DIMENSIONAL TOWARD A THREE-DIMENSIONAL STATE

The experimental results presented in the preceding section demonstrate the existence of different flow regimes characterized by different length and time scales. In this section, we want to gain a deeper insight into the features of the diverse flow structures illustrating the transition from a quasi-two-dimensional flow field to a three-dimensional one. At first, we want to discuss the role of Ekman pumping. Then, the results of our numerical simulations will be presented, rendering the details of the 3D velocity fields visible. Because of the limitation of the accessible values for Ra or Q, Ra was set to 3.0×10^4 and Q was reduced in order to increase the ratio Ra/Q in the simulations.

Temperature signal
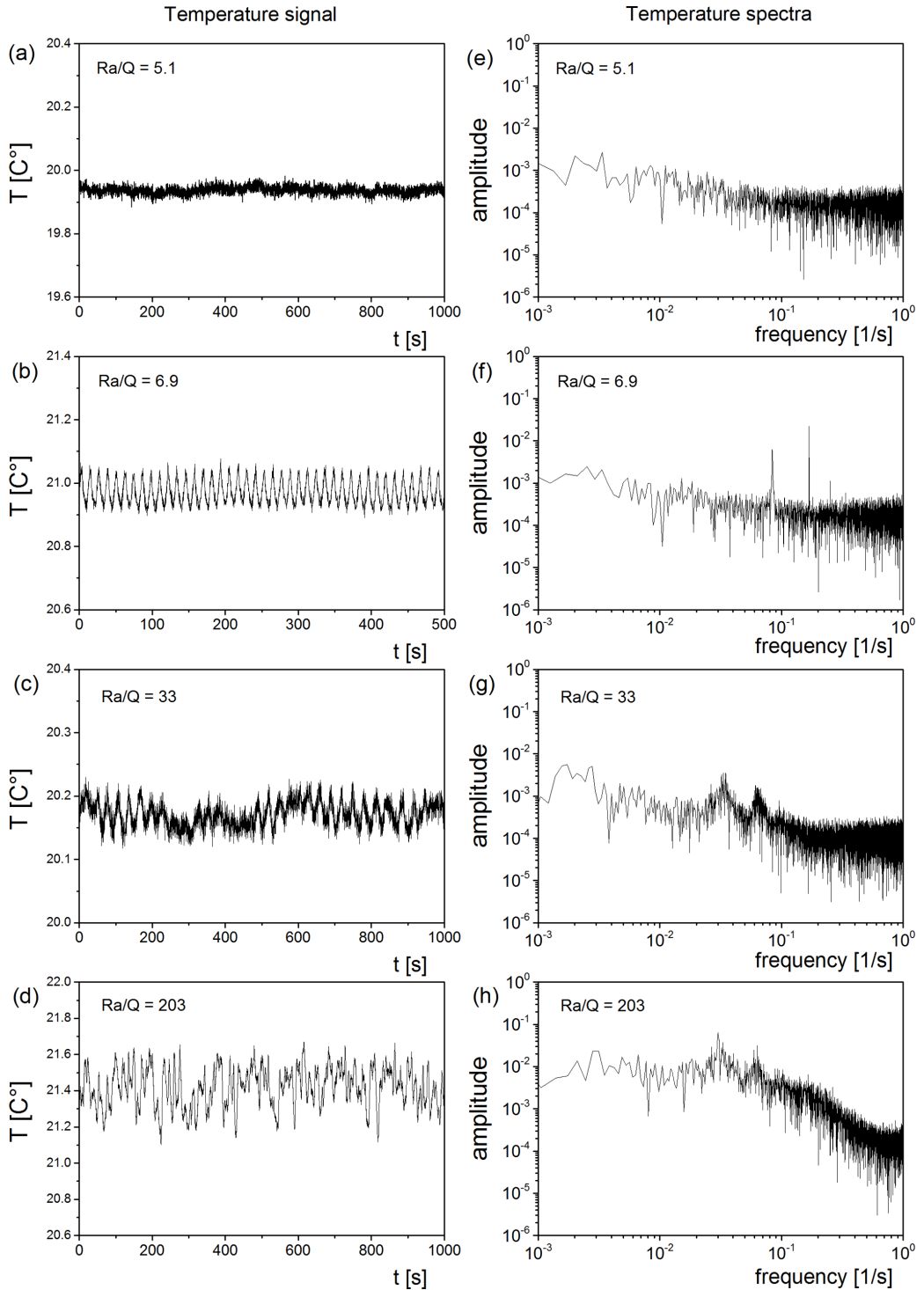
Temperature spectra

FIG. 7. Time series of the temperature (a)–(d) and temperature spectra (e)–(h) recorded simultaneously to the four flow measurements presented in Sec. III A: (a,e) $Ra/Q = 5.1$, (b,f) $Ra/Q = 6.9$, (c,g) $Ra/Q = 33$, and (d,h) $Ra/Q = 203$ (thermocouple position 2 in Fig. 1).
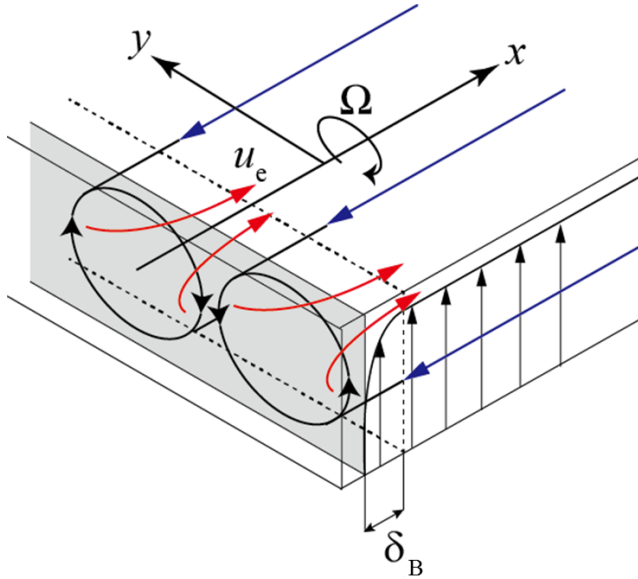
FIG. 8. Illustration of the axial flow forming due to Ekman-pumping along the convection rolls.

Selected cases with the same classification of flow regimes (short-OS, advective, and standing wave) will be shown referring to the experiments in Sec. III.

A. Steady rolls with superimposed axial flow: The relevance of Ekman pumping

The source of the axial flow component along the convection rolls (u_x) can be found in the boundary layers where the rolls touch the vessel walls. The imbalance between the centrifugal forces and the radial pressure gradient in the boundary layer drives the fluid radially inward and establishes, required by continuity, a secondary circulation as illustrated in Fig. 8, where u_e and δ_B indicate the characteristic velocity for Ekman pumping and the related Bödewadt boundary-layer thickness, respectively. Irrespective of the rotational direction, the direction of the secondary circulation in the steady state is such that the flow within the boundary layers is converging toward the axis of the convection roll. From here the fluid is pumped toward the midplane of the fluid vessel, and it streams back to the sidewalls along the rim of the convection rolls and within the space left between neighboring rolls forming two toroidal vortices along each convection roll. These vortices are symmetric with respect to the horizontal midplane of the fluid vessel. Consequently, this secondary flow is an inherent feature of any rotating flow that is confined by two parallel solid walls. The experimentally determined velocity data presented in Sec. III A are consistent with the schematic drawing in Fig. 8 whereby the different sensor positions explain the opposite sign of the flow patterns shown in Figs. 3(b) and 3(c). The path length of this Ekman-pumping-induced recirculation is about 2×100 mm for each circulation loop. The measurements presented in Fig. 3(b) allow an estimate of the average velocity of $\bar{u}_x = 0.4$ mm/s resulting in a recirculation time of approximately 500 s.

A similar secondary flow pattern was found by Pothérat *et al.* [23] for a columnar vortex that is locally driven at the wall by electromagnetic forces. In this situation, similar to a rotating disk, the maximum azimuthal velocities occur close to the wall and the resulting gradient of the swirl drives the secondary flow obviously in the opposite direction. The authors referred to this phenomenon as inverse Ekman pumping. Constantly changing boundary conditions can even lead to an intermittent behavior of the secondary flow [24].
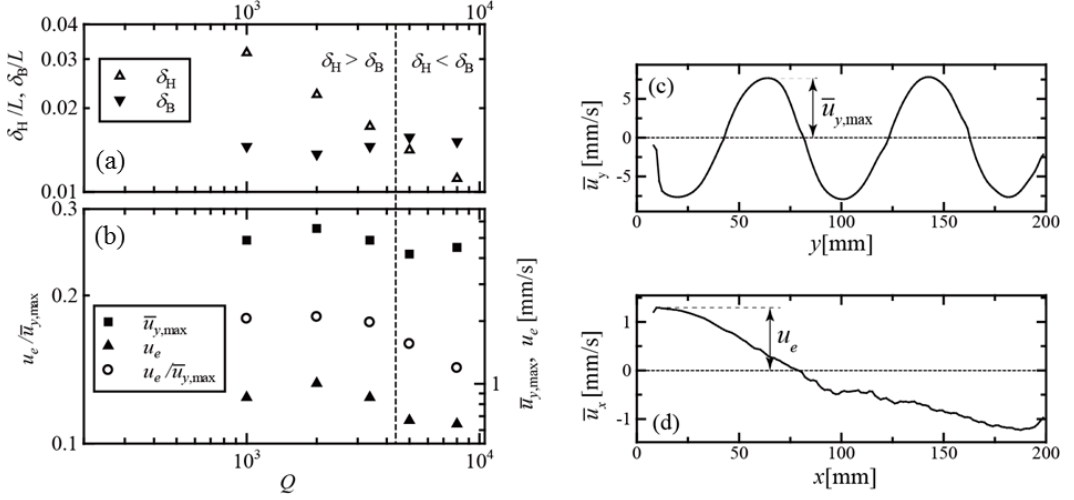
FIG. 9. (a) Variation of the thickness of the Bödewadt layer δ_B and the Hartmann layer δ_H vs the Q number; (b) characteristic velocities u_e, $\bar{u}_{y,\max}$ and the ratio $u_e/\bar{u}_{y,\max}$ vs the Q number; and time-averaged profiles of (c) the velocity perpendicular to the magnetic field, $\bar{u}_y(y)$ (Ch1), and (d) parallel to the magnetic field, $\bar{u}_x(x)$ (Ch4), for the case $Q = 2.0 \times 10^3$ and Ra $= 2.1 \times 10^4$.

In the case considered here, two boundary layers occur at the side walls perpendicular to the magnetic field, namely the Bödewadt layer $\delta_B = \sqrt{\nu/\Omega}$ (with the angular velocity $\Omega = \bar{u}_{y,\max}/r$, whereby $r = 10$ mm according to the measuring position) and the Hartmann layer $\delta_H = H/Q^{1/2}$. For sufficiently large Chandrasekhar numbers, the Hartmann layer is supposed to be considerably thinner than the Bödewadt layer.

Figure 9(a) compares the estimated thickness of the Bödewadt layer δ_B and the Hartmann layer δ_H for different experiments carried out for various Chandrasekhar numbers at a constant Ra number of Ra $\sim 2.1 \times 10^4$. It becomes obvious that for $Q > 4 \times 10^3$ the value for δ_H falls below δ_B. The representative velocity for the Ekman pumping flow, u_e, calculated from the experimental, time-averaged velocity profiles $\bar{u}_x(x)$, the typical rotating velocity of the convection rolls, $\bar{u}_{y,\max}$, and the ratio $u_e/\bar{u}_{y,\max}$, is shown in Fig. 9(b). The analysis is restricted to data corresponding to five-roll regimes in order to keep the relative position of the measurement line with respect to the convection rolls [also see Fig. 1(a)]. Figures 9(c) and 9(d) are examples of time-averaged velocity profiles, $\bar{u}_x(x)$ and $\bar{u}_y(y)$, obtained along the measurement lines Ch4 and Ch1, respectively [see Fig. 1(a)].

As expected from Fig. 9(a), a detectable reduction of $u_e/\bar{u}_{y,\max}$ can be noticed only for $Q > 4 \times 10^3$ where the Hartmann layer becomes thinner than the Bödewadt layer.

B. Occurrence of short-period oscillations

Figure 10(a) shows the roll structure obtained by a numerical simulation in a similar parameter range as in the experiment shown in Fig. 4, namely at $Q = 5.7 \times 10^3$, Ra $= 3.0 \times 10^4$, and Ra$/Q = 5.3$. Here, the convection rolls and side vortices are uncovered by isosurfaces of $Q_{3D} = 0$, the second invariant of the velocity gradient tensor. The criterion $Q_{3D} > 0$ indicates vortex-dominated regions [25], and it is widely utilized for identifying 3D flow structures. In this figure, five large counter-rotating convection rolls become visible. Another feature that can be recognized in this figure is the existence of additional smaller vortices. These vortices are elongated along the magnetic-field lines as well. Singular vortices can be found in the corner region of the cell while small pairs of counter-rotating vortices occur in the convergence zone of the neighboring convection rolls. Their location very close to the top and bottom of the fluid cell above and below the UDV-measuring lines is the reason why these smaller vortices cannot be seen in the velocity distribution shown in Fig. 4(a).
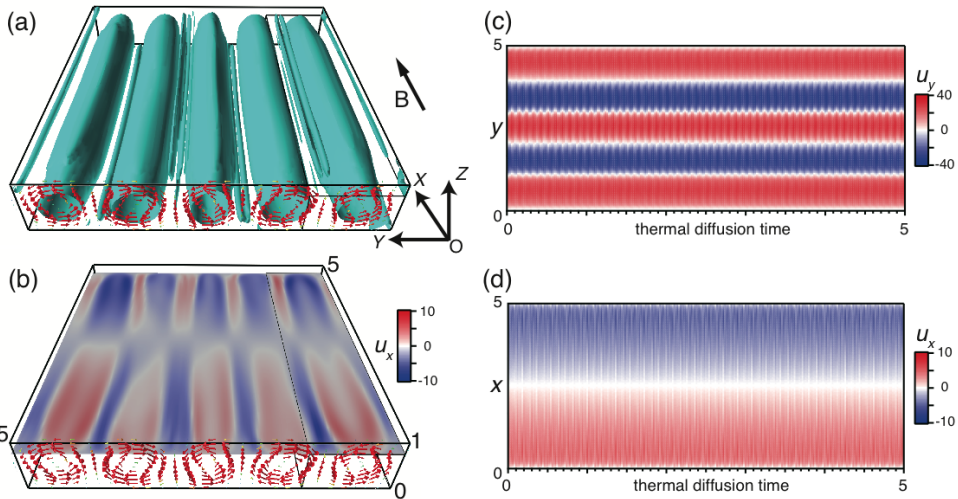
FIG. 10. Numerical simulation at $Q = 5.7 \times 10^3$, Ra $= 3.0 \times 10^4$ (Ra$/Q = 5.3$, five-roll short OS regime). (a) Isosurface of $Q_{3D} = 0$; (b) flow in the direction parallel to the magnetic field (u_x) on the plane $z = 3/4$; (c) velocity perpendicular to B on the y line at $x = 5/2$ and $z = 3/4$; (d) velocity parallel to B on the x line at $y = 5/4$ and $z = 3/4$; the location of the measuring line for (d) is indicated by a thin black frame in (a) and (b); see the Supplemental Material [26] for a movie of (a).

The small side vortices play an important role in the stability of the considered flow because such a configuration is supposed to cause flow oscillations and transition to turbulence, as will be shown below. Instabilities of these small elongated vortices and their interaction with the convection rolls can be considered as a reason for a deformation of the initially circular roll cross section. Such a deformation becomes apparent in the form of the short-period flow oscillation in the flow measurements. The roll deformation is visible in Fig. 10(a). For a better visualization of the roll deformation and how this roll deformation rotates around the roll axis, we refer the reader to the Supplemental Material (movie) [26]. It can be seen here that the flow structure is still almost two-dimensional.

The Ekman pumping, which is responsible for the flow components parallel to B, is demonstrated in Fig. 10(b) in terms of the spatial distribution of the u_x velocities at $z = 3/4$. Obviously, this figure obtained by numerical simulations provides a more detailed visualization of the Ekman-induced recirculation compared to the UDV-line measurements. The axial inflow inside the convection rolls occurs over a wide radial range. The return flow toward the walls can be observed in the region between neighboring convection rolls. The inflow is separated from the return flow by sharp shear layers.

Figures 10(c) and 10(d) contain the numerical counterpart to the measured spatiotemporal contour plots presented in Fig. 4. The linear velocity profiles were determined for the same positions where the ultrasonic sensors were installed at the experimental setup. Here, the time axis is based on the thermal diffusion time $\tau_\kappa = H^2/\kappa$. If the nondimensional values are adapted to the experiment, the value of u_y is ± 7.9 mm/s, that of u_x is ± 1.5 mm/s, and the frequency of the oscillation is 0.074 Hz. These slightly different values compared to the case in Fig. 4 can be explained by the smaller Ra number used in the simulation. The typical ratio between the velocities in u_y and u_y is 0.18, which is consistent with the measurements. The qualitatively good agreement between the numerical findings and the experimental results confirms the reliability of our numerical approach convincingly.

C. Transition to 3D structures

In Fig. 5, we showed a measurement obtained at a higher value of Ra$/Q = 33$ where small vortices were detected moving in the u_x velocity field. The appearance of these vortices can be taken as an
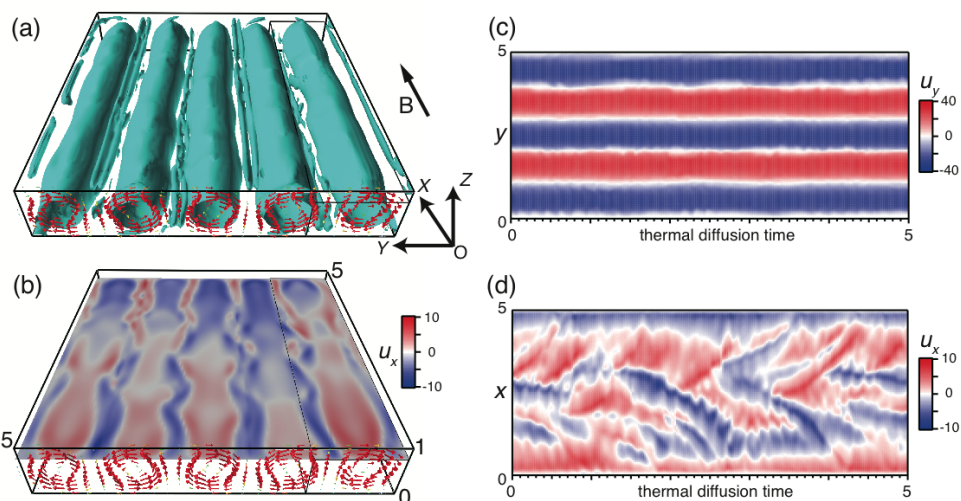
FIG. 11. As in Fig. 10, but obtained at $Q = 3.23 \times 10^3$, Ra $= 3.0 \times 10^4$ (Ra$/Q = 9.3$, five-roll advective regime); see the Supplemental Material [26] for a movie of (a).

indication of the transition from a quasi-two-dimensional to a three-dimensional flow structure in a very early state. In this section, we want to reveal the characteristic flow structures occurring during this transition. Moreover, our findings demonstrate that the decreasing impact of the Lorentz force (indicated by the growing Ra$/Q$ value) results both in a gradual loss of the two-dimensionality in the flow pattern and an increasingly turbulent convection.

Figure 11(a) shows a snapshot of the vortex structure (isosurfaces at $Q_{3D} = 0$) for a weakly transitional convection at Ra$/Q = 9.3$. This figure illustrates the incipient destabilization of the convection. It can be seen that the small intermediate vortices become unstable and partially interrupted. The perturbation of the small vortices goes along with further deformations of the convection rolls. Now, the recirculating flow induced by Ekman pumping [see Fig. 11(b)] becomes effective by propagating such perturbations along the x direction parallel to the magnetic field. This becomes obvious in the movie in Ref. [26] and in Fig. 11(d), whereby Figs. 11(c) and 11(d) show the temporal evolution of this transitional flow at the corresponding UDV measuring lines. Again, the numerical outcome bears a close resemblance to the experimental results shown in Fig. 5. It is worth noting that the ratio Ra$/Q$ for Fig. 11 is much smaller than that of Fig. 5, which might be attributed to the difference in the number of rolls (five and four). Migrating local structures appearing near the center of the vessel as displayed in Fig. 5(b) and also in Fig. 11(d) cannot be distinguished in the vortex structure shown in Fig. 11(a). But, the mapping of the axial flow in a horizontal plane at $z = 3/4$ [Fig. 11(b)] shows the formation of local perturbations near the center. In this moment, the Ekman pumping flow is no longer symmetric with respect to the vessel center line at $x = 5/2$. The perturbations appearing in both Figs. 5(b) and 11(d) are obviously generated around the central region of the vessel and move alternatingly to the opposite sides. Our estimations show that the propagation speed of the local structures arising from a deformation of the main rolls and the destabilization of the small aligned vortex pairs corresponds well to the velocity of the Ekman pumping flow. These features are characteristic for transitional flows and produce the complex patterns that were observed in the axial velocity map.

The Chandrasekhar number is reduced in Fig. 12 to study a further step toward the transition to turbulent convection. Here, a numerical simulation is presented for $Q = 1.76 \times 10^3$, Ra $= 3.0 \times 10^4$(Ra$/Q = 17$). In Fig. 12(a), one can see the formation of small vortices just above the convection rolls, whereas its rotational axis is aligned almost perpendicularly with respect to the direction of the convection roll axis. Figure 12(b) shows the u_x velocity field at $z = 3/4$, and Figs. 12(c) and 12(d)
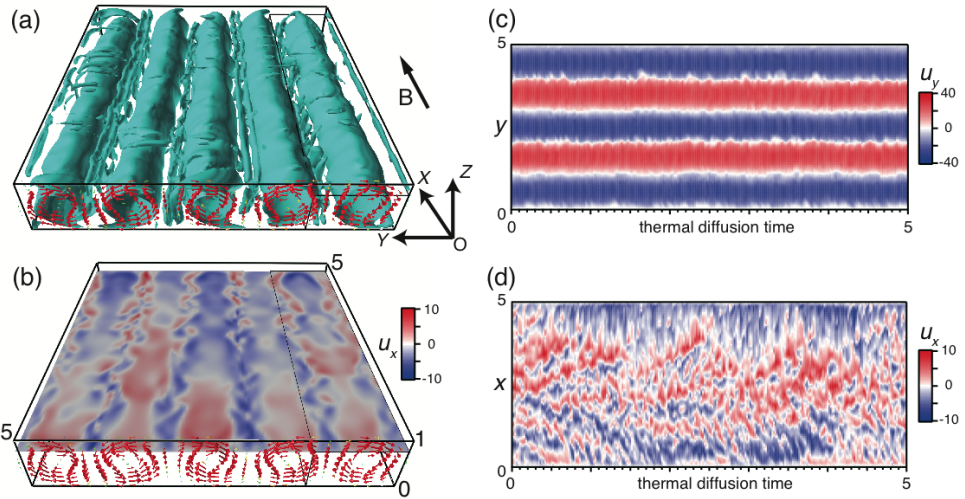
FIG. 12. As in Fig. 10, but obtained at $Q = 1.76 \times 10^3$, Ra $= 3.0 \times 10^4$ (Ra/$Q = 17.0$, five-roll advective regime); see the Supplemental Material [26] for a movie of (a).

shows the temporal evolution of u_y and u_x, respectively. While the pattern of the primary convection rolls still looks quite stable in time [Fig. 12(c)], the increasing number of subvortices becomes apparent in Fig. 12(d). It is hardly possible to determine the origin of these small vortices by means of these contour plots, but a corresponding movie [26] indicates that the vortices detach from the small aligned vortex pairs between the primary rolls. These fragments become stretched and wrapped around the primary rolls. Moreover, they are affected by the roll deformation and the disturbed secondary flow driven by Ekman pumping [see Fig. 12(b)]. As a result, Fig. 12(d) shows a very complex pattern of the flow velocity parallel to B. The comparison between Figs. 12 and 11 suggests that the difference in the related flow states is not substantial, however the increasing fragmentation of the small aligned vortex pairs and their entrainment into the rotating flow of the convection rolls lead to the rather complex velocity map of u_x shown in Fig. 12(d). Apparently, the deformation of the convection rolls plays an important role in the transition to turbulence. This deformation might be caused by a Kelvin-Helmholtz instability arising from the shear flow between Ekman pumping and its return flow generating alternating small vortices around the center of the vessel, or an oscillatory instability of the main rolls as known from the standard Rayleigh-Bénard convection.

A further decrease of Q leads to the flow pattern shown in Fig. 13. The size of the side vortices increases, and the tendency to a growing disorder in the flow structure becomes more and more pronounced. The convection rolls are subject to rather strong oscillations but still show the known basic structure of the four-roll regime [Fig. 13(c)]. The structure resembles the structure that exists when standing waves occur. Figure 13(a) and the animation of the numerical results [26] reveal a recurrent bulging of the rolls in the direction perpendicular to the magnetic field. The roll deformation has, of course, a significant effect on the side vortices, which form now almost closed vortex tubes winding around the convection rolls. The interaction between these vortices and convection rolls is much stronger than in the previous examples.

The occurrence of a standing wave is also verifiable in the u_x velocity field of the secondary flow shown in Fig. 13(d). The phenomenon is quite similar to that discovered by flow measurements in Fig. 6. The simulations reveal that Ekman pumping no longer forms continuous loops covering the entire fluid vessel; instead, the secondary circulation is confined to local patches near the wall. This phenomenon is immediately understood when one recalls that the secondary flow in the form of Ekman pumping is driven by the axial gradient of the swirling flow. Due to the clear deformation
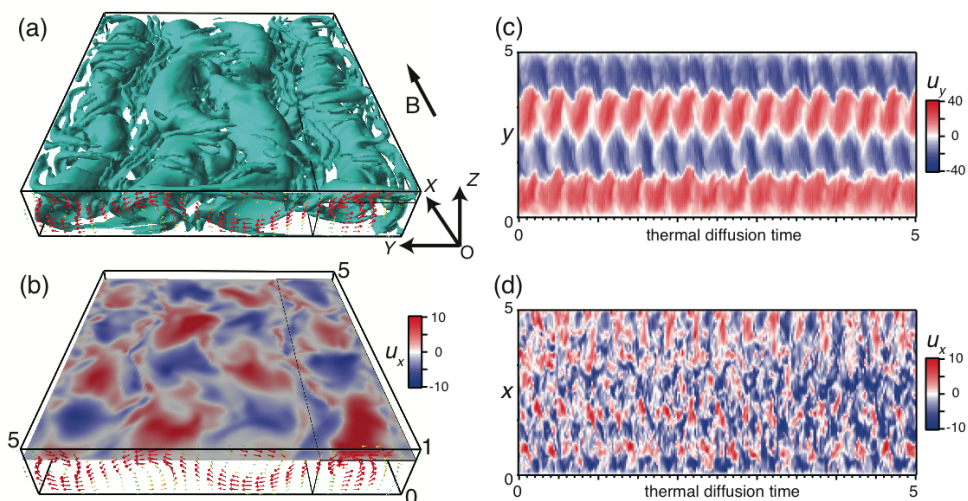
FIG. 13. As in Fig. 10, but obtained at $Q = 6.25 \times 10^2$, $Ra = 3.0 \times 10^4$ ($Ra/Q = 64.0$, four-roll standing-wave regime); see the Supplemental Material [26] for a movie of (a).

of the convection rolls, this gradient changes a few times along the roll axis in the x direction. As a result, the original recirculation loop breaks down into several smaller cells.

V. DISCUSSION AND CONCLUSIONS

The present paper considers the specific case of Rayleigh-Bénard convection (RBC) inside an electrically conducting fluid exposed to a horizontal dc magnetic field. For this specific case of liquid-metal convection, we performed successful velocity measurements in the direction of the magnetic field. For that purpose, we used special custom-built ultrasonic transducers that are not affected by the strong magnetic field. The principal effect of the magnetic field is a reorientation of the convection toward a quasi-2D configuration where counter-rotating convection rolls are aligned with the magnetic-field lines. This work focuses on changes toward an increasingly 3D flow structure occurring as a consequence of a gradual decrease of the magnetic-field strength.

A very satisfactory result of this study is the fact that the complex three-dimensional flow structures found in the flow measurements can also be reproduced by the numerical simulations. Although the parameters characterizing the distinctive flow pattern in the experiment and the numerical data are not exactly identical and there is no perfect agreement with respect to the quantitative data, the numerical calculations provide a very detailed description of the flow morphology and give an intuitive understanding of the corresponding mechanisms.

The rotating flow in a quasi-2D convection roll between two parallel solid walls is always accompanied by Ekman pumping creating a secondary flow. Inside the Bödewadt boundary layers, the fluid is pumped toward the rotational axis of the convection rolls. The fluid then leaves the boundary layer in the interior of the convection roll and creates a recirculation parallel to the magnetic-field lines. Two symmetrical recirculation zones can be found in each convection roll. The magnitude of this circulation is about 1/5 of the rotation speed of the rolls. An increase of Q results in a thinning of the Hartmann layer ($\delta_H \sim Q^{-1/2}$) arising thereby a dominating influence of Joule dissipation. A weakening of the flow becomes visible once the Hartmann layer thickness falls below the thickness of the Bödewadt layer.

As a key issue, in this paper we addressed the question of how the stability of the quasi-two-dimensional flow structure is affected when the Chandrasekhar number is gradually reduced. The declining magnetic-field effect enables the development of diverse flow oscillations, which can

be attributed to two-dimensional variations of the roll structure and emerging 3D flow effects. In particular, short- and long-period oscillations occur that can be detected both in the velocity and the temperature field. The frequency of the short-period temperature oscillations is identical to the frequency that can be deduced from the velocity field. The analysis of data obtained by measurements of the axial flow component discloses that the flow regime showing short oscillations of the primary roll structure can be subdivided into two regimes. The short-period oscillations appear if the shape of the convection rolls deviate from their original circular cross section. Here, the main flow structure still remains quasi-two-dimensional for sufficiently strong magnetic fields ($\mathrm{Ra}/Q < 10$). With increasing Ra/Q ratio ($\mathrm{Ra}/Q \geqslant 30$), distinct deviations from two-dimensionality can be detected at first in the secondary flow driven by Ekman pumping. Small-scale swirling substructures emerge in the flow structure measured along the magnetic-field lines. These perturbations are captured by the secondary recirculation and transported toward the Bödewadt-Hartmann walls of the fluid vessel. In line with this, the time scales of the long-period oscillations are in the order of the Ekman recirculation time. Our numerical simulations show that the long-period oscillations are related to roll deformations in axial direction of the convection rolls. This newly discovered regime was called the four- or five-roll advective regime. The detailed onset conditions and the mechanism behind the oscillations are rather complex and will be addressed in a future work.

The transition to fully three-dimensional flow further proceeds by an increase of Ra/Q to values around 100. Here, we observed a new three- or four-roll standing-wave regime. This regime appears at a certain Ra/Q ratio where the previously magnetic-field-aligned side vortices become unstable, change their orientation, and wind around the convection rolls. Afterward, these vortices follow Ekman-induced recirculation and move toward the sidewalls of the vessel. The numerical simulations demonstrated that the secondary flow created by Ekman pumping can no longer form continuous loops covering the entire fluid vessel. Here, the secondary circulation is restricted to local patches near the side walls of the fluid vessel. The spatiotemporal plots of the flow pattern derived from both the experiment and the numerical calculations reveal the features of a standing wave of the convection rolls in this regime.

Another topic, which is reserved for later work, concerns the scaling law for identifying the actual point in the regime diagram where the transition between quasi-2D and -3D flows occurs. Within the scope of this study, it was clearly demonstrated that a growing value of the ratio Ra/Q results in an increasing dominance of three-dimensional flow structures. It is well known from many studies dealing with MHD channel flows or flows in liquid-metal layers that the magnetic interaction $N = Q/\mathrm{Re}$ is another important parameter (see, for instance, [15,18,27–29]). According to [30], the application of a dc magnetic field causes the flow to become two-dimensional at a certain point when the so-called true interaction parameter $N_t = N(l_\perp/l_\parallel)^2$ exceeds a value of 1, where $l_\perp$ and $l_\parallel$ denote the characteristic size of the flow structure in the directions perpendicular and parallel to the magnetic-field lines, respectively. In this study, the exact point where the two-dimensional state of an oscillating flow becomes three-dimensional was not determined. Therefore, there remains a well-founded answer to this question for subsequent research.

The results in this paper clearly demonstrate that the flow structure of the RBC in a horizontal magnetic field can already become three-dimensional even if the measurements perpendicular to the magnetic field still suggest a stable two-dimensional structure of the primary convection rolls. The deviations from two-dimensionality become apparent first in the secondary flow driven by Ekman pumping. Although the presented effects arising from the secondary flow are often weak compared to the primary convection rolls, their impact on the global flow field and the transition to three-dimensional turbulent flows is essential.

[1] G. Ahlers, S. Grossmann, and D. Lohse, Heat transfer and large scale dynamics in turbulent Rayleigh-Bénard convection, Rev. Mod. Phys. **81**, 503 (2009).

[2] F. Chillà and J. Schumacher, New perspectives in turbulent Rayleigh-Bénard convection, Eur. Phys. J. E **35**, 58 (2012).

[3] U. Burr and U. Müller, Rayleigh-Bénard convection in liquid metal layers under the influence of a horizontal magnetic field, J. Fluid Mech. **453**, 345 (2002).

[4] J. M. Aurnou and P. L. Olson, Experiments on Rayleigh-Bénard convection, magnetoconvection and rotating magnetoconvection in liquid gallium, J. Fluid Mech. **430**, 283 (2001).

[5] E. M. King, S. Stellmach, J. Noir, U. Hansen, and J. M. Aurnou, Boundary layer control of rotating convection systems, Nature (London) **457**, 301 (2009).

[6] E. M. King and J. M. Aurnou, Turbulent convection in liquid metal with and without rotation, Proc. Natl. Acad. Sci. USA **110**, 6688 (2013).

[7] T. Zürner, W. Liu, D. Krasnov, and J. Schumacher, Heat and momentum transfer for magnetoconvection in a vertical external magnetic field, Phys. Rev. E **94**, 043108 (2016).

[8] S. Chandrasekhar, *Hydrodynamic and Hydromagnetic Stability* (Oxford University Press, Oxford, 1961).

[9] M. R. E. Proctor and N. O. Weiss, Magnetoconvection, Rep. Prog. Phys. **45**, 1317 (1982).

[10] S. C. Kakarantzas, A. P. Grecos, N. S. Vlachos, I. E. Sarris, B. Knaepen, and D. Carati, Direct numerical simulation of a heat removal configuration for fusion blankets, Energy Convers. Manage. **48**, 2775 (2007).

[11] T. Yanagisawa, Y. Hamano, T. Miyagoshi, Y. Yamagishi, Y. Tasaka, and Y. Takeda, Convection patterns in a liquid metal under an imposed horizontal magnetic field, Phys. Rev. E **88**, 063020 (2013).

[12] T. Yanagisawa, Y. Yamagishi, Y. Hamano, Y. Tasaka, and Y. Takeda, Spontaneous flow reversals in Rayleigh-Bénard convection of a liquid metal, Phys. Rev. E **83**, 036307 (2011).

[13] T. Yanagisawa, Y. Hamano, and A. Sakuraba, Flow reversals in low-Prandtl-number Rayleigh-Bénard convection controlled by horizontal circulations, Phys. Rev. E **92**, 023018 (2015).

[14] Y. Tasaka, K. Igaki, T. Yanagisawa, T. Vogt, T. Zuerner, and S. Eckert, Regular flow reversals in Rayleigh-Bénard convection in a horizontal magnetic field, Phys. Rev. E **93**, 043109 (2016).

[15] P. A. Davidson, Magnetic damping of jets and vortices, J. Fluid Mech. **299**, 153 (1995).

[16] V. W. Ekman, On the influence of the earth's rotation on ocean-currents, Arkiv Matem., Astronom. Fys. **2**, 1 (1905).

[17] V. U. Bödewadt, Die Drehströmung über festem Grunde, ZAMM-J. Appl. Math. Mech./Z. Angewandt. Math. Mech. **20**, 241 (1940).

[18] J. Sommeria and R. Moreau, Why, how, and when, MHD turbulence becomes two-dimensional, J. Fluid Mech. **118**, 507 (1982).

[19] P. A. Davidson and A. Pothérat, A note on Bödewadt-Hartmann layers, Eur. J. Mech. B/Fluids **21**, 545 (2002).

[20] N. T. Baker, A. Pothérat, and L. Davoust, Dimensionality, secondary flows and helicity in low-Rm MHD vortices, J. Fluid Mech. **779**, 325 (2015).

[21] Y. Plevachuk, V. Sklyarchuk, S. Eckert, G. Gerbeth, and R. Novakovic, Thermophysical properties of the liquid Ga-In-Sn eutectic alloy, J. Chem. Eng. Data **59**, 757 (2014).

[22] T. Vogt, I. Grants, D. Räbiger, S. Eckert, and G. Gerbeth, On the formation of Taylor-Görtler vortices in RMF-driven spin-up flows, Exp. Fluids **52**, 1 (2012).

[23] A. Pothérat, F. Rubiconi, Y. Charles, and V. Dousset, Direct and inverse pumping in flows with homogeneous and non-homogeneous swirl, Eur. Phys. J. E **36**, 94 (2013).

[24] C. Zhang, V. Shatrov, J. Priede, S. Eckert, and G. Gerbeth, Intermittent behaviour caused by surface oxidation in a liquid metal flow driven by a rotating magnetic field, Metall. Mater. Trans. B **42**, 1188 (2011).

[25] J. C. R. Hunt, A. A. Wray, and P. Moin, Eddies, streams, and convergence zones in turbulent flows, Center for Turbulence Research Report No. CTR-S88 (1988), p. 193.

[26] See Supplemental Material at http://link.aps.org/supplemental/10.1103/PhysRevFluids.3.013503 for movies for Figs. 10–13(a) and an indication of time variations of structure by the isosurface of $Q_{3D} = 0$. The time duration for these movies is one thermal diffusion time.

[27] J. Sommeria, Electrically driven vortices in a strong magnetic field, J. Fluid Mech. **189**, 553 (1988).

[28] R. Klein and A. Pothérat, Appearance of Three-Dimensionality in Wall Bounded MHD Flows, Phys. Rev. Lett. **104**, 034502 (2010).

[29] S. Eckert, G. Gerbeth, W. Witke, and H. Langenbrunner, MHD turbulence measurements in a sodium channel flow exposed to a transverse magnetic field, Int. J. Heat Fluid Flow **22**, 358 (2001).

[30] B. Sreenivasan and T. Alboussiere, Experimental study of a vortex in a magnetic field, J. Fluid Mech. **464**, 287 (2002).